Model of human low-density lipoprotein and bound receptor based on CryoEM

Gang Ren[a,b,1], Gabby Rudenko[c], Steven J. Ludtke[b], Johann Deisenhofer[d], Wah Chiu[b,1], and Henry J. Pownall[e,1]

[a]Department of Biochemistry & Biophysics, University of California, San Francisco, San Francisco, CA 94158; [b]National Center for Macromolecular Imaging, Verna and Mars McLean Department of Biochemistry and Molecular Biology; [e]Section of Atherosclerosis and Vascular Medicine, Department of Medicine, Baylor College of Medicine, Houston, Texas 77030; [c]Life Sciences Institute and Department of Pharmacology, University of Michigan, Ann Arbor, MI 48109; and [d]Howard Hughes Medical Institute and the Department of Biochemistry, The University of Texas, Southwestern Medical Center at Dallas, Dallas, Texas 75390.

Edited by Richard J. Havel, Cardiovascular Research Institute, San Francisco, CA, and approved November 30, 2009 (received for review July 17, 2009)

Human plasma low-density lipoproteins (LDL), a risk factor for cardiovascular disease, transfer cholesterol from plasma to liver cells via the LDL receptor (LDLr). Here, we report the structures of LDL and its complex with the LDL receptor extracellular domain (LDL · LDLr) at extracellular pH determined by cryoEM. Difference imaging between LDL · LDLr and LDL localizes the site of LDLr bound to its ligand. The structural features revealed from the cryoEM map lead to a juxtaposed stacking model of cholesteryl esters (CEs). High density in the outer shell identifies protein-rich regions that can be accounted for by a single apolipoprotein (apo B-100, 500 kDa) leading to a model for the distribution of its α-helix and β-sheet rich domains across the surface. The structural relationship between the apo B-100 and CEs appears to dictate the structural stability and function of normal LDL.

apolipoprotein B-100 | cholesteryl ester | electron cryomicroscopy | LDL receptor

Low-density lipoproteins (LDL), which are heterogeneous with respect to composition, shape, size, density, and charge (1, 2), are the major carriers of cholesterol in human plasma. LDL is removed from plasma by hepatic LDL receptors (LDLr), which maintain cholesterol homeostasis (3). LDLr variants with impaired binding to LDL cause familial hypercholesterolemia that leads to premature atherosclerotic coronary artery disease in affected patients (4). The extracellular domain of LDLr binds to LDL via apo B-100, a 4,536 amino acid polypeptide, after which the complex (LDL · LDLr) undergoes endocytosis, lysosomal degradation of LDL, and receptor recycling to the cell surface (1, 3, 4). Thus, interactions between LDL and LDLr are integral to the cholesterol homeostasis that regulates plasma LDL levels.

LDL exhibits a thermal liquid crystalline-to-isotropic transition of its cholesteryl esters (CEs) between 25 and 35 °C (5). Although several models of LDL attempt to integrate its structure and biology (5–9), a reliable three-dimensional structure of LDL or the LDL · LDLr complex has not yet been reported. Herein, we present a model of LDL and the complex, LDL · LDLr, of LDL-bound LDL receptor extracellular domain (1–699 a.a.) at extracellular pH determined by electron cryomicroscopy (cryoEM), a technique that preserves the native structure of the particles.

Result and Discussion

CryoEM micrographs of LDL embedded in vitreous ice contain spherical, ellipsoidal, and discoidal particles with internal striations (Fig. 1*A* and *B*). Since the LDL preparation is heterogeneous, our reconstruction was computed from ∼8,500 particle images of LDL particles that were computationally selected from an original pool over ∼48,000 particle images. The convergence of the structure from this subpopulation of particle images provides a statistically defined and robust density map displaying the most prominent and reliable structural features of LDL (Fig. 1*C*, and Figs. S1, 2). The reconstructed LDL subpopulation is approximately a flattened ellipsoid with planar opposing faces (∼250 Å × ∼240 Å × ∼166 Å). The shape is oval when viewed from the top. The planar top and bottom surfaces are parallel and ∼166 Å apart. Lateral views of LDL reveal an approximately rounded trapezoid with grooves on the front and back surfaces (Fig. 1*C* bottom).

Notably, the other ∼40,000 particle images are qualitatively similar to the selected subpopulation, but tend to be somewhat larger or rounder in appearance. We also observed larger particles with additional striations. While the protein content of LDL is fixed, the amount of triglyceride, lipids, and cholesterol varies. Nothing in the images of these other particles invalidates our analysis of the subpopulation,, but due to the large variability within the set, and the use of one orientation in the imaging, we cannot produce other reliable three-dimensional structures from these data. Proper characterization of the heterogeneity within this population may use a technique like electron cryotomography followed by posttomographic classification, alignment, and averaging (10).

The features observed in raw micrographs of the LDL · LDLr complex are essentially identical to those of LDL, except for the appearance of an additional high-density protrusion on the surface (Fig. 1*D*, *E*). The reconstructed map of the LDL · LDLr complex is also similar to that of LDL, containing the same shape and dimensions as LDL with an additional ∼35–45 Å protrusion on the surface (Fig. 1*F*). The size and location of this protrusion corresponds well to the additional high-density region observed in raw micrographs of the LDL · LDLr complex (Fig. 1*E* left). The dimensions of the protrusion determined from a difference map (Fig. 2, gold mesh) is most compatible with that of the LDL receptor β-propeller with a part of EGF-like repeat C domain, a ∼40 kDa domain with a diameter of ∼40–50 Å as seen in its crystal structure (11) (Fig. 2, red). Though the LDLr location is clear, its orientation is ambiguous due to the roundness of the density. In contrast, the cysteine-rich repeats and EGF-like repeats are much smaller (11 to 15 Å each based on C_α distances). Moreover, the cysteine-rich repeats or EGF-like repeats are unlikely to interact with each other to form a larger module because at neutral pH the LDLr extracellular domain is elongated (11–13) and at acidic pH these modules interact with each other only via their linker regions (11). While LDL binding to LDLr certainly in-

Author contributions: G.Ren, G.R., J.D., W.C., and H.J.P. designed research; G.Ren performed research; G.Ren, G.R., S.J.L., J.D., and H.J.P. contributed new reagents/analytic tools; G.Ren analyzed data; G.Ren, G.R., W.C., and H.J.P. wrote the paper.

The authors declare no conflict of interest.

This article is a PNAS Direct Submission.

Freely available online through the PNAS open access option.

Data deposition: The cryo-EM density maps LDL and LDL.LDLr are available from the EMDB as EMDB ID 5153 and 5158, respectively.

[1]To whom correspondence should be addressed. E-mail: hpownall@bcm.tmc.edu or wah@bcm.edu or gren@msg.ucsf.edu.

This article contains supporting information online at www.pnas.org/cgi/content/full/0908004107/DCSupplemental.

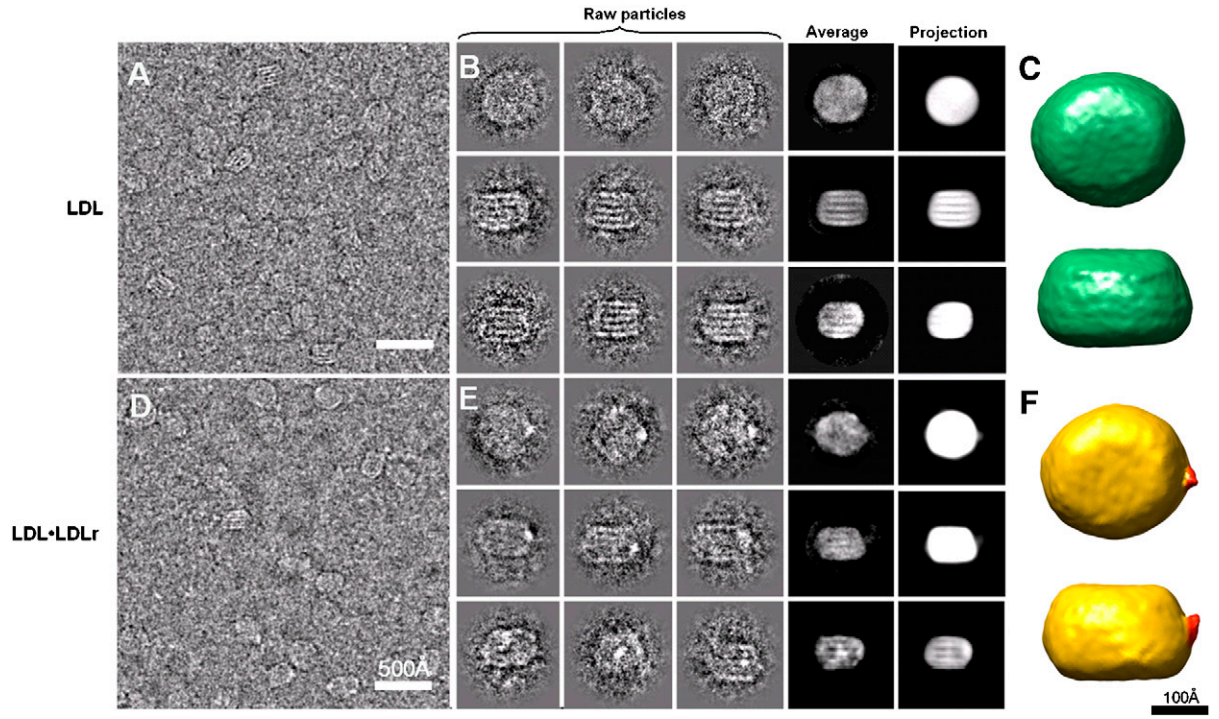

Fig. 1. CryoEM structure of LDL alone and bound to receptor. (*A*) A representative area of a CCD image of LDL particles embedded in vitreous ice. Particles are circular or oval, the latter often containing striations. (*B*) Three representative views of selected and windowed raw particles of LDL (*left* column) and their class averages (*center* column) are compared with their corresponding views of the same projections in a three dimensional density map of LDL (*right* column). (*C*) Three-dimensional density map of LDL reveals an ellipsoidal shape with flat opposing surfaces (*green* at 1.2σ). (*D*) Representative view of a CCD image of ice-embedded LDL · LDLr complexes. (*E*) Three views of selected and windowed raw LDL · LDLr complexes (*left* column), their class averages (*center* column), and their projections in a three-dimensional density map (*right* column). (*F*) The three-dimensional density map of LDL · LDLr (*gold* at 1.92σ) shows a discoidal shape similar to that of LDL except for an additional protrusion (highlighted in red) on one side.

volves cysteine-rich repeats of the ligand binding domain because their deletion reduces binding to <20% of the wild-type LDLr, two studies support the hypothesis that at neutral pH the β-propeller also interacts with lipoproteins, because receptors with amino acid substitutions in the β-propeller bind less ligand than wild-type LDLr (13, 14).

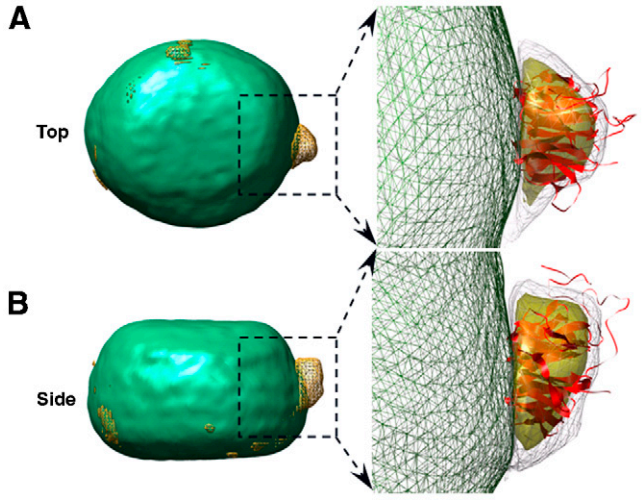

Fig. 2. Difference map of LDL and LDL · LDLr. A difference map (*gold* net) between the three-dimensional density maps of LDL · LDLr and LDL is superimposed onto the LDL map (*green* solid) and shown in perpendicular views in (*A*) and (*B*). The major peak in the difference map is a nose-shaped protrusion on the surface of LDL (*green* net) with dimensions ~60 Å × ~47 Å × ~30 Å at a contour level of 0.92σ (*gray* mesh) and ~45 Å × ~35 Å × ~23 Å at 1.3σ (*gold* transparent density). Superposition of the LDLr β-propeller domain plus a part of EGF-like repeat C from the crystal structure of the ectodomain (PDB: 1N7D, residues G375—A699, red) into the difference map reveals its location.

The internal density distribution of LDL shows an organized core. To examine the internal core, density maps of LDL and LDL · LDLr were cut into halves along two orthogonal directions perpendicular to the plane of the top surface (Fig. 3*A* and *C*). By contouring the cross sections from low-density (3.04σ, in blue) to high-density (6.84σ, in red) using a color ramp scheme, the cut-away surfaces display three flat, internal higher-density regions (green striations), which are parallel to each other and to the highest density planar top surfaces (yellow, orange, and red). Much lower density and chambers (blue and gray holes) appear on both sides of these high-density internal striations. The three internal high densities form what are roughly three-layers of "isthmi" with similar dimensions. The density near the center of each "isthmus" is stronger than that near the edges. The isthmi are parallel to each other and separated by ~35 Å. The two outer isthmi are also parallel to the outer shell of LDL, at a distance of ~31 Å.

We propose a liquid crystalline core model of LDL in which the CE molecules are arranged in stacks with their sterol moieties side-by-side in the higher-density regions while the fatty acyl chains extend from either side, and are observed as parallel lower-density compartments (Fig. 3*B*, *D*). Indeed our model builds on the early report of LDL as a discoidal, i.e., non spherical particle with apoB in two ring-shaped structures around the perimeter (15). Later studies using image reconstruction showed LDL as more spheroidal than discoidal and the presence of striations (16) but with less detail than in the present study where we observe a non uniform distribution of high and low density that we assign to protein- and lipid-rich surface regions respectively. Unlike the earlier structure (16), in the present study the

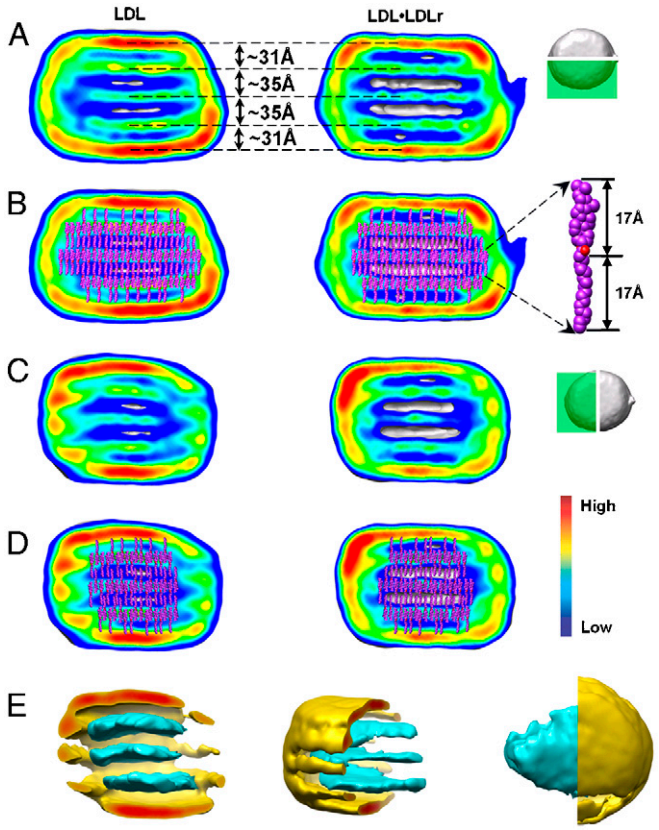

Fig. 3. The structure of the LDL internal CE core. (*A*) Cut-away surface views of the three-dimensional density maps of LDL (*left*) and the LDL · LDLr complex (*right*). Both cores contain striations separated by ~35 Å at the center of the particle and ~31 Å near the surface. (*B*) The cores largely comprise CEs, which are modeled as juxtaposed stacks. In this model, the high density sterol moieties of the CE molecules (*magenta*) are coplanar and their acyl chains extend outwards on either side into parallel planes that form the four lower density compartments. (*C*) and (*D*) show corresponding views perpendicular to (*A*) and (*B*) respectively. Similar features are seen including the low density gaps demonstrating that the internal striations span the whole core, and accommodate CE in coplanar layers. (*E*) Three different views of the internal structure of the core showing the "isthmi" density map (contoured at 4.0σ, *cyan*) and the high density outer surface shell (contoured at 5.32σ, *yellow*). The scale on right indicates increasing density at contour levels of 3.04σ (*blue*), 4.0σ (*cyan*), 4.75σ (*green*), 5.13σ (*yellow*), and 6.84σ (*red*).

contrast transfer function (CTF) of the microscope has been fully corrected so that the core and edge are properly connected.

According to the core dimensions observed here and the partial specific volume of CE (17), the striated core can accommodate ~1200 CE molecules. Calculations based on LDL composition give a similar value, ~1400 (18, 19). The additive length of the longest dimension of cholesterol (~17 Å) and an 18-carbon acyl chain (~17 Å) is ~34 Å, which is consistent with the X-ray scattering measurements (19). The dimensions of CE are compatible with a juxtaposed stacking model of CEs (Fig. 3), with the sterol moieties spaced at ~34 Å. The smaller spacing (~31 Å) seen near the periphery is likely due to the protein elements of the outer shell, for example the ~8 Å-thick β-sheet-rich domain, being thinner than the 17 Å sterol moiety and because the smaller number of acyl chains in the outer stack of sterol moieties permits some acyl chain tilting. Our model is completely different from an earlier model of LDL deduced from x-ray scattering experiments suggesting that CE molecules were distributed in concentric radial shells with their sterol moieties aligned side-by-side (19).

The density of LDL, 1.03–1.06 g/ml is derived from the weighted average of its high-density component, protein, and the low-density components, lipids (17). Phospholipids and protein each comprise about half of the surface components of LDL. Thus, the LDL density map is expected to contain regions of different densities that correspond to the apo B-100 and the lipids respectively. To reveal the high density regions in the three-dimensional map of LDL, we display the map at two contour levels, 5.67σ (yellow solid) and 4.76σ (green mesh; Fig. 4*A*). At a higher contour level of 5.67σ, we assign the corresponding region to be that of apo B-100, e.g. ~18% of entire LDL volume. At a slightly lower contour level of 4.76σ, the map volume is about twice that of the apo B-100 volume and is a reasonable estimation of apo B-100 with bound phospholipids. These two contour levels together reveal an apo B-100 configuration that appears as a pair of paddles (Fig. 4*A*, top and bottom faces), connected at one end of the particle by a linker region (Fig. 4*A*, right and left faces), with three separate semicircular and long "fingers" extending from each edge of the linker region to wrap around the particle (Fig. 4*A*, front and back faces). These fingers have similar lengths (~230 Å) and are separated by at least ~35 Å. Notably, the finger-shaped densities on the "front" are weaker than on the back suggesting that the front region is lipid-rich and distinct from the rest of the particle surface. Thus, the overall shape of the high density surface features suggests that the apo B-100 molecule comprises top and bottom paddles that are attached by a linking region, with a railing of semicircular fingers on each side.

According to sequence-based structural predictions, apo B-100 can be divided into five domains, including two amphipathic β-sheet rich (β_1, β_2), two amphipathic α-helix rich (α_2, α_3), and a mixed α-β domain $(\beta\alpha_1)$ (Fig. 4*D*). Each α-helix-rich domain comprises more than 500 amino acid residues that are predicted to form 4–5 unusually long single α-helices (80–240 Å each, Fig. S3). The β-sheet rich domains are predicted to have more than ~80% of their residues forming β-strands or loops. Similar analysis led previously to the so-called pentapartite model of apo B-100 (20), but the spatial distributions of these five domains on the LDL particle have remained unassigned. In general, a low-resolution map cannot resolve the structural motifs of a protein. However in our case, we can assign the spatially discrete high-density regions of the map to domains in the pentapartite model, i.e. the α-helix rich and β-sheet rich domains by considering: (*i*) the unusual structural motifs of apo B-100 with several unusually long α helices in the two α-helix rich domains, (*ii*) the consensus that the apo B-100 is distributed throughout the surface of the particle (5, 7, 9), and lastly (*iii*) the scattering density difference between protein and lipids, (Fig. 4 *B*, *C*). In our model, the paddles (top and bottom faces) and linker (right face) comprise the amphipathic β-sheet domains, and the railings of semicircular fingers (front and back faces) contain the amphipathic α-helices. The continuous amphipathic β-sheets domains, β_1 and β_2, are likely anchored to the core lipids via their hydrophobic faces, with few if any interspersed phospholipids. The more flexible α_2 and α_3 domains containing multiple stretches of α-helices likely orient their amphipathic helical axes coplanar to the surface monolayer of phospholipids as seen in the front and back of the particle. The stacks of acyl chains in the CE core are directed outward towards the amphipathic β-sheets domains on the top and bottom faces of the particle (Fig. 4*B* and *D*) and are semicircular surrounded by the flexible amphipathic α-helix rich domains (Fig. 4*E*). According to this model and the reconstructed maps (Figs. 3 and 4), the LDLr β-propeller domain binds to the linker between the amphipathic β-sheets domains that comprise the top and bottom paddles (Fig. 4*A*, right, asterisk). This assignment is consistent with the biochemical data of others. The apoB antibodies 4G3, 278, 3G9, and 5E11 which block LDL binding to its receptor (21, 22) are known to bind apoB residues in the region containing amino acids 3000–3500, a region that the pentapartite model of

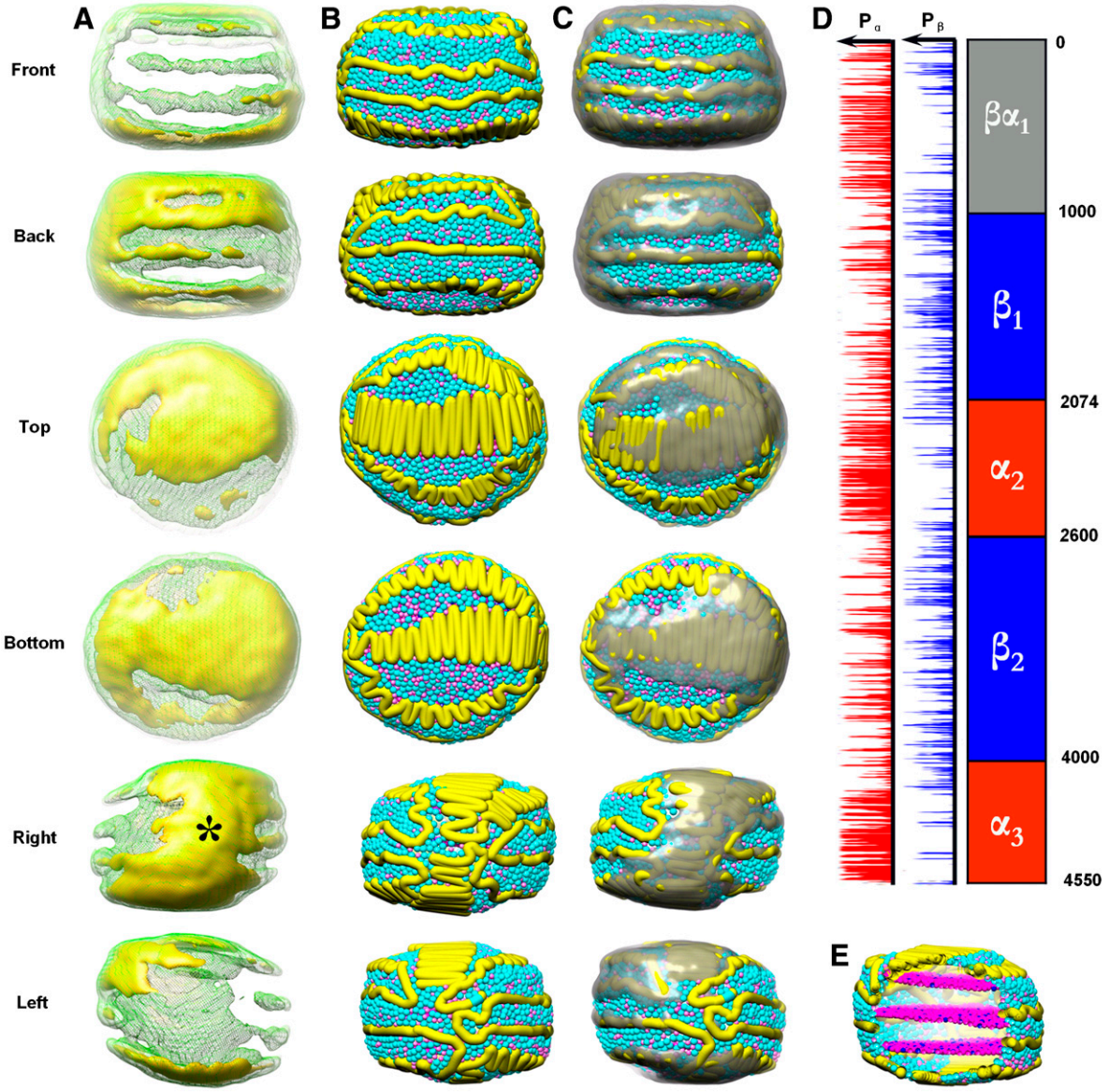

Fig. 4. High density outer features of LDL reveal the structure of apoB-100. (*A*) Six orthogonal views are shown. The high density region of the LDL three-dimensional map is displayed at the contour level of 5.67σ (*yellow*) and 4.76σ (*green* mesh). The lowest density features of the outer shell map to the 'front' and 'left' views. The asterisk in the 'right' view indicates the location of the putative β-propeller of the LDLr. (*B*) Six orthogonal projection views of the pentapartite model of apo B-100 (two amphipathic β-sheet rich domains interrupted by two amphipathic α-helix-rich domains, shown in *yellow* cable) onto the three-dimensional reconstruction of LDL. (*C*) Superposition of the high outer shell density (*beige* translucent solid), i.e., apo B-100 from (*A*) and the domain structure of the pentapartite model (*yellow* cable) from (*B*). (*D*) Probability ($P = 0$, low; $=1$, high) of helical (*red*, P_α) and β-strand (*blue*, P_β) regions in apo B-100 based on sequence prediction suggests a five domain model designated as α_2, α_3, β_1, β_2 and $\beta\alpha_1$. (*E*) A cut-away view of the LDL model shows the surface structure of apo B-100 and the internal organization of the CE sterol moieties. In (*B*), (*C*), and (*E*), the phospholipid head groups, CE, and TG are displayed as *cyan*, *magenta*, and *blue* balls respectively.

apoB predicts to be a β-sheet domain. The cryoEM reconstruction of the LDL · LDLr complex localizes the β-propeller to a β-sheet domain (β_1 or β_2) of the pentapartite model of LDL as well (Fig 4, asterisk). Our finding is thus consistent with the biochemical studies using antibodies. However, since the cryoEM map is low-resolution, we cannot with confidence discriminate between β_1 and β_2 in assigning their locations to specific densities.

Our model reveals not only protein-rich regions but also protein-poor, lipid-rich regions (Fig. 4*A* left face) that are potential sites where enzymes and lipid transfer proteins could interact with the phospholipid surface via their putative interfacial recognition sites. The most notable of these is cholesteryl ester transfer protein, which transports CE from HDL to LDL and very low-density lipoprotein (VLDL), and is known to bind to phospholipid surfaces that contain no protein (23).

Our structure was obtained after quenching from below the LDL thermal transition temperature so that most particles were captured in a liquid crystalline phase. A similar study with LDL quenched from 37 °C would likely produce fewer liquid crystalline LDL particles. Nevertheless, our structure is likely relevant to LDL physiology. The major determinant of the transition temperature is the triglyceride content, which is lowest ($4.5 \pm 0.4\%$) for the middle density fraction (2), which was used in our study. Because of the breadth of the transition there is still a fraction of LDL that is liquid crystalline even at 37 °C. In addition, in the liver the triglyceride content of LDL could be further lowered by hepatic lipase (24) thereby increasing the number of liquid

crystalline particles in vivo. Finally, the surface densities defined by the distribution of protein and lipid in LDL particles containing an isotropic liquid core are likely to share some similarities with our structure, although this will have to be experimentally verified.

Our model of apo B-100 and CE packing is consistent with many biochemical and biophysical measurements (5, 6, 16–19, 21–23, 25, 26), and divides apo B-100 into multiple domains that surround a core with a distinctive liquid crystalline structure. The structural organization between CE and apo B-100 may bear relevance to human pathobiology. While normal individuals have a predominance of large LDL particles, some patients have an atherogenic lipoprotein phenotype that is characterized by small, dense LDL particles; this phenotype is associated with low plasma HDL-cholesterol, insulin resistance, and increased risk for coronary heart disease (27). Unlike the core of normal LDL which is liquid crystalline (Fig. 3), the small, dense LDL is triglyceride-enriched and has an isotropic liquid core with no apparent striations according to cryoEM (18). Furthermore, the apo B-100 of triglyceride-rich LDL also shows impaired binding to fibroblast LDL receptors, suggesting an altered conformation (28, 29). Thus, there is compelling evidence that the structure of the LDL core stabilizes the conformation of apo B-100 that interacts with its receptor and with the vascular endothelium. The similar separation of the finger-like densities of apo B-100 (Fig. 4) and the periodicity of CE isthmi (Fig. 3) observed in our cryoEM structure suggest that the surface apo B-100 structure follows that of the liquid crystalline core and their spatial relationship is important to maintain the structural integrity and thus functionality of the normal LDL. Future studies of LDL from hypertriglyceridemic subjects should shed light on the structures associated with impaired cellular LDL uptake.

Materials and Methods

Isolation of LDL. LDL (density = 1.006–1.063 g/mL), isolated by sequential flotation of plasma from a fasted, healthy male volunteer, was further purified according to density by isopycnic density gradient ultracentrifugation in TBS (50 mM Tris-HCl buffer, 150 mM NaCl, pH 7.5) (2). The central fraction, D4, (density = 1.043 g/mL) was collected and dialyzed against 10 mM Tris pH 7.4, 100 mM NaCl, 0.5 mM EDTA. The LDL protein concentration was determined with a commercial kit (BioRad DC Assay) using BSA as a standard. LDL was stored at 4 °C under nitrogen gas and vitrified within 14 d.

LDL · LDLr Complex. The hexa-histidine tagged extracellular domain of wild-type human LDLr (a.a. 1–699, ~80 kDa) was overexpressed in insect cells (11). To form the LDL · LDLr complex, a 1 : 2 molar ratio of LDL to LDLr (200 μg LDL and 80 μg LDLr) was combined in 800 μL to final concentrations 0.25 and 0.1 μg/μL respectively in 20 mM Tris pH 8, 100 mM NaCl, 0.5 mM $CaCl_2$. After incubating for 30 min at 4 °C, the sample was passed through a 500 Å pore-size filter (Osmonics) to remove aggregates. Complex formation was verified by spinning the LDL · LDLr complex reaction in 100 kDa cut-off centrifugal filtration device, which showed that LDLr in presence of LDL was retained while LDLr without LDL passed through filter.

CryoEM Specimen Preparation. LDL in 25 mM Tris pH 7.4, 100 mM NaCl, 0.5 mM EDTA was diluted to 0.05 μg/μL in 10 mM Tris buffer and used to prepare EM grids. Undiluted LDL · LDLr complex (0.25 μg/μL LDL) was diluted 1 : 2 and 1 : 4 into 20 mM Tris pH 8, 100 mM NaCl, 0.5 mM $CaCl_2$. Microscope specimens were prepared on Quantifoil (Quantifoil Micro Tools GmbH) holey carbon film-coated 400 mesh copper grids. The grids were glow discharged for 1 min before incubating with 4 μL LDL or LDL · LDLr complex (0.05 μg/μL LDL). The samples were frozen at 100% humidity and 4 °C using a Vitribot rapid-plunging device (FEI) and blotted with filter paper (#595, Schleicher & Schuell GmbH) for 2 sec. The frozen, hydrated specimens were transferred to liquid nitrogen for storage until viewing by cryoEM.

CryoEM Data Collection. Micrographs of LDL and LDL · LDLr particles were acquired at liquid helium temperature (4-25 ° Kelvin) using a JEM3000SSF electron cryomicroscope (JEOL) with a field emission gun operated at 300 kV high tensions. The microscope was equipped with a Gatan US4000 4k × 4k CCD camera (Gatan) with a condenser aperture of 100 μm, a spot size of three and an objective lens aperture of 70 μm. Images of LDL were recorded with a microscope magnification of ~40, 000×, a dose of ~20 $e^-/Å^2$, and a defocus of 1.5 to 3.5 μm; those of LDL · LDLr complex were recorded similarly but with a Gatan 2K x2K CCD camera at a microscope magnification of 50, 000×.

Image Processing. Individual particle images were selected using the program *boxer* in the EMAN package (30). A total of 47,593 particles were picked automatically and manually checked to remove overlapped particles or damaged particles from 654 LDL CCD frames with a 112 × 112 pixel box (~476 Å × 476 Å at the specimen); 12,547 particles were boxed from 275 LDL · LDLr complex CCD frames, using a 192 × 192 pixel box (~518.4 Å × 518.4 Å at the specimen). CTF and envelope-function parameters were fitted using the automated fitting program *fitctf.py* and subsequently manually adjusted by *ctfit* (EMAN suite; (30)). *Applyctf* (EMAN suite) was used to apply phase corrections to the particles and store CTF parameters for later amplitude correction. For LDL and the LDL · LDLr complex, 1,969 and 1,268 class averages were used respectively.

Three-Dimensional Reconstruction. To prevent bias from a starting model, a smooth 297 Å × 270 Å × 243 Å Gaussian blob was generated by *makeinitialmodel.py* and used for refinement during reconstruction of both LDL and the LDL · LDLr complex models. For the beginning eight refinement rounds, only very low-resolution information for the particles was used (below the first CTF zero in reciprocal space). Iterative refinement proceeded until convergence. For higher resolution refinement, CTF amplitude correction was performed, finer angular sampling was used, and solvent flattening via masking was imposed. This process was iterated until convergence as well. According to the 0.5 Fourier shell correlation criterion (31), the final resolutions of the asymmetric reconstructions for LDL and the LDL · LDLr complex were ~28 Å.

Structural Analysis. Visualization and segmentation of the three-dimensional reconstructions were performed using UCSF Chimera (32). The LDL maps were analyzed at different contour levels based on the estimated volumes of the total LDL particle (3.87×10^6 $Å^3$) and the volume of apo B-100 (6.46×10^5 $Å^3$). To analyze the LDL · LDLr complex, the final LDL reconstruction was scaled and aligned to the final LDL · LDLr complex reconstruction and a difference map calculated using *proc3d* (30). To locate the LDLr on the LDL surface, the β-propeller domain with a part of EGF-like repeat C domain from the crystal structure of the extracellular domain of the LDLr (PDB ID: 1N7D, residues Gly 375—Ala 699, a total of 325 residues or 2,450 atoms) (11) was automatically docked to the difference map between the LDL · LDLr complex and LDL, and contoured at 1.3σ. The protein secondary structure predictive algorithm, PredictProtein (33), was used to determine the probability (P) of apo B-100 regions forming an α-helix (P_α) or β-strand (P_β). The distribution of these regions of secondary structure has been used to generate a pentapartite model of apo B-100.

ACKNOWLEDGMENTS. Ren thanks D.A. Agard, K.H. Weisgraber at UCSF and M.F. Schmid at Baylor College of Medicine for discussions.This project has been supported by the Biomedical Technology Research Center for Structural Biology (P41RR02250) and P01GM99116; Rudenko was supported by an American Heart Scientist Development Award. Ren was partially supported by W.M. Keck Foundation. Pownall was supported by HL-30914 and -56865.

1. Havel RJ, Goldstein JL, Brown MS (1980) Lipoproteins and Lipid Transport. *The Metabolic Control of Disease*, ed Rosenberg PBaL (W.B. Saunders Company, Philadelphia) p 398.
2. Gaubatz JW, et al. (2007) Dynamics of dense electronegative low density lipoproteins and their preferential association with lipoprotein phospholipase A(2). *J Lipid Res*, 48 (2):348–357.
3. Brown MS, Goldstein JL (1986) A receptor-mediated pathway for cholesterol homeostasis. *Science*, 232(4746):34–47.
4. Hobbs HH, Brown MS, Goldstein JL (1992) Molecular genetics of the LDL receptor gene in familial hypercholesterolemia. *Hum Mutat*, 1(6):445–466.
5. Deckelbaum RJ, Shipley GG, Small DM, Lees RS, George PK (1975) Thermal transitions in human plasma low density lipoproteins. *Science*, 190(4212):392–394.
6. Spin JM, Atkinson D (1995) Cryoelectron microscopy of low density lipoprotein in vitreous ice. *Biophys J*, 68(5):2115–2123.
7. Segrest JP, Jones MK, De Loof H, Dashti N (2001) Structure of apolipoprotein B-100 in low density lipoproteins. *J Lipid Res*, 42(9):1346–1367.
8. Johs A, et al. (2006) Modular structure of solubilized human apolipoprotein B-100. Low resolution model revealed by small angle neutron scattering. *J Bio Chem*, 281 (28):19732–19739.

9. Krisko A, Etchebest C (2007) Theoretical model of human apolipoprotein B100 tertiary structure. *Proteins*, 66(2):342–358.
10. Schmid MF, Booth CR (2008) Methods for aligning and for averaging 3D volumes with missing data. *J Struct Biol*, 161(3):243–248.
11. Rudenko G, et al. (2002) Structure of the LDL receptor extracellular domain at endosomal pH. *Science*, 298(5602):2353–2358.
12. Zhao Z, Michaely P (2008) The epidermal growth factor homology domain of the LDL receptor drives lipoprotein release through an allosteric mechanism involving H190, H562, and H586. *J Biol Chem*, 283(39):26528–26537.
13. Yamamoto T, Chen HC, Guigard E, Kay CM, Ryan RO (2008) Molecular studies of pH-dependent ligand interactions with the low-density lipoprotein receptor. *Biochemistry*, 47(44):11647–11652.
14. Huang S, Henry L, Ho YK, Pownall HJ, Rudenko G (2009) Mechanism of LDL Binding and Release Probed By Structure-Based Mutagenesis of the LDL Receptor. *J Lipid Res.* In press.
15. Van Antwerpen R, Gilkey JC (1994) Cryo-electron microscopy reveals human low density lipoprotein substructure. *J Lipid Res*, 35(12):2223–2231.
16. Orlova EV, et al. (1999) Three-dimensional structure of low density lipoproteins by electron cryomicroscopy. *Proc Natl Acad Sci USA*, 96(15):8420–8425.
17. Tardieu A, et al. (1976) Structure of human serum lipoproteins in solution II. Small-angle x-ray scattering study of HDL3 and LDL. *J Mol Biol*, 105(3):459–460.
18. Sherman MB, Orlova EV, Decker GL, Chiu W, Pownall HJ (2003) Structure of triglyceride-rich human low-density lipoproteins according to cryoelectron microscopy. *Biochemistry*, 42(50):14988–14993.
19. Atkinson D, Deckelbaum RJ, Small DM, Shipley GG (1977) Structure of human plasma low-density lipoproteins: molecular organization of the central core. *Proc Natl Acad Sci USA*, 74(3):1042–1046.
20. Segrest JP, Jones MK, Mishra VK, Anantharamaiah GM, Garber DW (1994) apoB-100 has a pentapartite structure composed of three amphipathic alpha-helical domains alternating with two amphipathic beta-strand domains. Detection by the computer program LOCATE. *Arterioscler Thromb*, 14(10):1674–1685.
21. Milne R, et al. (1989) The use of monoclonal antibodies to localize the low density lipoprotein receptor-binding domain of apolipoprotein B. *J Biol Chem*, 264(33): 19754–19760.
22. Swenson TL, Brocia RW, Tall AR (1988) Plasma cholesteryl ester transfer protein has binding sites for neutral lipids and phospholipids. *J Biol Chem*, 263(11):5150–5157.
23. Deckelbaum RJ, Shipley GG, Small DM (1977) Structure and interactions of lipids in human plasma low density lipoproteins. *J Biol Chem*, 252(2):744–754.
24. Aviram M, Lund-Katz S, Phillips MC, Chait A (1988) The influence of the triglyceride content of low density lipoprotein on the interaction of apolipoprotein B-100 with cells. *J Biol Chem*, 263(32):16842–16848.
25. Wang X, Pease R, Bertinato J, Milne RW (2000) Well-defined regions of apolipoprotein B-100 undergo conformational change during its intravascular metabolism. *Arterioscl Throm Vas*, 20(5):1301–1308.
26. Shen BW, Scanu AM, Kezdy FJ (1977) Structure of human serum lipoproteins inferred from compositional analysis. *Proc Natl Acad Sci USA*, 74(3):837–841.
27. Berneis KK, Krauss RM (2002) Metabolic origins and clinical significance of LDL heterogeneity. *J Lipid Res*, 43(9):1363–1379.
28. McKeone BJ, Patsch JR, Pownall HJ (1993) Plasma triglycerides determine low density lipoprotein composition, physical properties, and cell-specific binding in cultured cells. *J Clin Invest*, 91(5):1926–1933.
29. Aviram M, Bierman EL, Chait A (1988) Modification of low density lipoprotein by lipoprotein lipase or hepatic lipase induces enhanced uptake and cholesterol accumulation in cells. *J Biol Chem*, 263(30):15416–15422.
30. Ludtke SJ, Baldwin PR, Chiu W (1999) EMAN: semiautomated software for high-resolution single-particle reconstructions. *J Struct Biol*, 128(1):82–97.
31. Bottcher B, Wynne SA, Crowther RA (1997) Determination of the fold of the core protein of hepatitis B virus by electron cryomicroscopy. *Nature*, 386(6620):88–91.
32. Pettersen EF, et al. (2004) UCSF Chimera—a visualization system for exploratory research and analysis. *J Comput Chem*, 25(13):1605–1612.
33. Rost B, Yachdav G, Liu J (2004) The PredictProtein server. *Nucleic Acids Res*, 32(Web Server issue):W321–326.

Supporting Information

Ren et al. 10.1073/pnas.0908004107

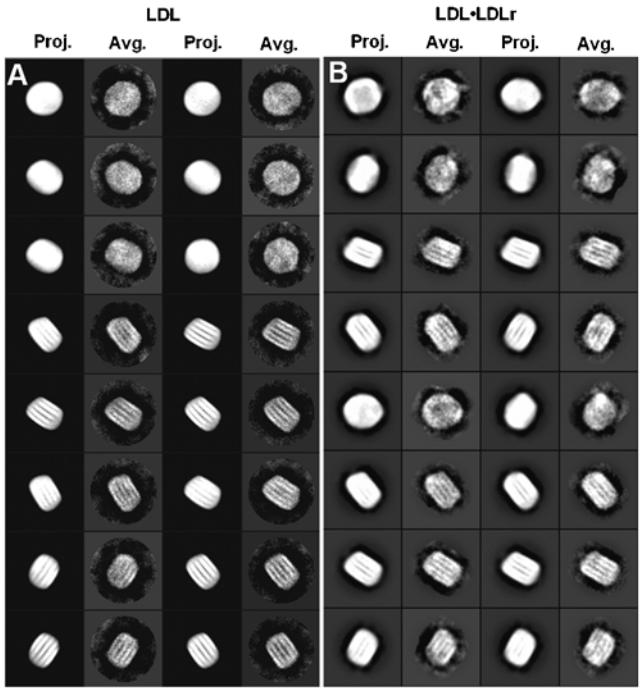

Fig. S1. Single-particle image reconstruction of LDL and LDL · LDLr complexes. Selected reference projections of the final three-dimensional reconstruction (*A*, *left*, projection) versus corresponding class averages (*B*, *right*, average) of LDL (*left*) and LDL · LDLr (*right*).

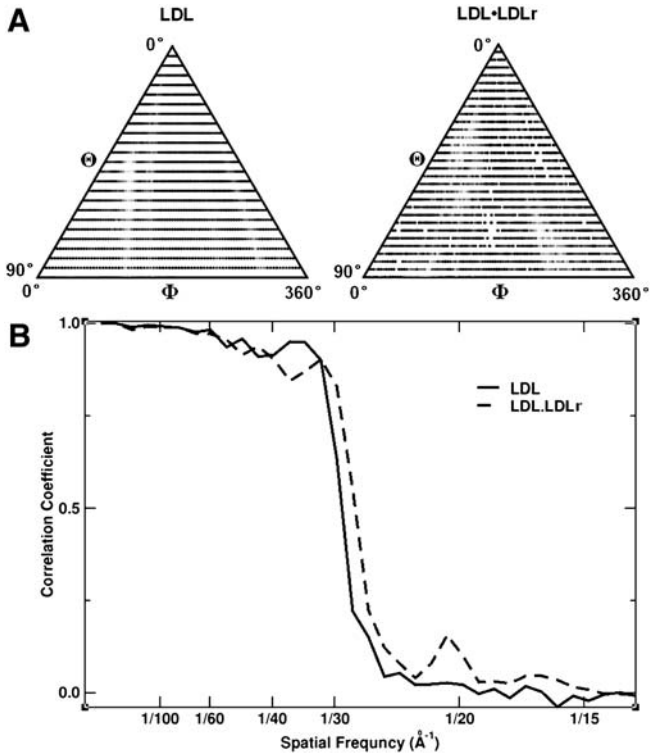

Fig. S2. Single-particle image reconstruction of LDL and LDL · LDLr complexes. (*A*) Histogram of the raw images in each view of the final model showing that all views of the LDL (*left*) and LDL · LDLr (*right*) complex are well represented and that there are no obvious preferential orientations. Images were aligned translationally (*x* and *y*) and rotationally in-plane (ω), and each particle was assigned to the group to which it correlated best. Each circle represents a projection of the final model for a given Θ and Φ value. (*B*) Fourier shell correlation to determine map resolution. The total dataset of images was divided into two equal groups, the particles in each dataset were aligned independently with projections of the final model, and two independent maps were correlated in Fourier space. The curves cross the 50% threshold at 28 Å resolution for LDL and LDL · LDLr reconstructions.

Fig. S3. Sequence-based structure prediction of two α-helix rich domains, α_2 and α_3. (*A*) The analysis suggests the α_2 domain contains six unusually long helices (highlighted in red), which are ≈90 Å long (60 a.a.), ≈78 Å (52 a.a.), ≈75 Å (50 a.a.), ≈237 Å (158 a.a.), ≈35 Å (~23 a.a.), and ≈63 Å (95 a.a.), respectively. In total, 438 out of 520 a.a. (≈90%) are involved in alpha helical structure. (*B*) Similarly, the α_3 domain contains 8 α-helices. The length of the helices are about ≈65 Å (43 a.a.), ≈87 Å (58 a.a.), ≈61 Å (40 a.a.), ≈87 Å (58 a.a.), ≈98 Å (65 a.a.), ≈87 Å (58 a.a.), ≈92 Å (61 a.a.), and ≈37 Å (25 a.a.), respectively. In total ≈82% of the ≈500 a.a. residues comprising the α_3 domain can be assigned to α-helices. The short helices are mostly near the beginning or ending portion of both α-domains which are highlighted in gray and green. The small loops between long helices are highlighted in purple.